Romanian Reports in Physics **75**, 504 (2023)

FORMATION AND DETECTION OF SECONDARY CRYSTALLINE PHASES IN Cu_2SnS_3 THIN FILMS FOR PHOTOVOLTAIC APPLICATIONS

D. CATANA[1], C. A. PARLOAGA[1], M. Y. ZAKI[2], D. SIMANDAN[2],
A. T. BURUIANA[1,2], F. SAVA[2], A. VELEA[2,*]

[1] Faculty of Physics, University of Bucharest, Atomistilor 405, 077125, Magurele, Romania
[2] National Institute of Materials Physics, Atomistilor 405A, 077125, Magurele, Romania
[*] Corresponding author: *alin.velea@infim.ro*

Received July 18, 2023

Abstract. Cu_2SnS_3 thin films emerged as promising materials for sustainable photovoltaics due to their earth-abundant constituents and great optoelectronic properties. The formation of secondary phases during synthesis poses challenges to achieving efficient performances. This study investigates the impact of secondary phases on the properties of CTS films.

Key words: Cu_2SnS_3, secondary phases, photovoltaics.

DOI: https://doi.org/10.59277/RomRepPhys.2023.75.504

1. INTRODUCTION

Thin films solar cells (TFSC) have become some of the main research hotspots in the environmentally friendly arena for photovoltaic applications. Due to their earth – abundant constituents, low manufacturing costs and non-toxicity, Cu_2SnS_3 (CTS) emerged as promising alternatives for absorber layer replacements in TFSC technology [1, 2]. Chalcogenide-based materials, such as CTS, exhibit thermal and aqueous stability along with desirable optoelectronic properties. However, drawbacks in achieving high conversion performance appear due to concentrated harmful structural defects [3]. Under different synthesis conditions, CTS can be found in 3 different crystalline phases, cubic, monoclinic and tetragonal [4]. As a precursor of the CZTS family [5] of composite thin films, the ternary Cu_xSnS_y can be regarded as a leap forward in terms of feasibility purposes in the photovoltaic technology and, fortunately the energy industry sector. The occurrence of different secondary phases in CTS thin films during the synthesis and post–deposition annealing process can severely impact the optoelectronic properties and subsequently the efficiency of the further assembled solar cell. By conducting qualitative studies on the formation of secondary phases, the optical, morphological and compositional properties of the thin film structures can be enhanced.

With an optimal band gap ranging from 0.8 to 1.7 eV [6], next to charge carrier – related advantages provided by their p-type semiconductor inherent nature [7, 8], CTS materials offer a wide range of utility and versatility in the photovoltaics production research industry. The achieved bandgaps make CTS suitable for absorber layers application for thin film solar cells [9]. One of the main drawbacks that requires extensive theoretical and experimental studies is their relatively low power conversion efficiency (PCE) of around 12–13% [10] compared to older and less eco-friendly thin films solar cells technologies like CIGS and organic solar cells acing between 23–24%, respectively 17–20% PCE [11, 12], respectively. The PCE of CTS is the subject of thorough research for systematic improvement. The occurrence of additional secondary phases can represent a halt in attaining the desired stoichiometry and morphological properties considered necessary for superior results.

Different physical and chemical methods have been utilized for the fabrication of CTS films, such as pulsed laser deposition (PLD) [13], chemical bath deposition (CBD) [14], thermal evaporation [15], spray pyrolysis [16] and magnetron sputtering [17]. Amongst these techniques, magnetron sputtering is one of the most versatile physical vapour deposition techniques used in thin film manufacturing investigations [18]. A series of magnetron configurations allow for a broad range of applications and optimization potential in the materials science sector [19]. By providing a homogeneous material coating with high-quality adhesion to the substrate and enhanced maneuverability of the deposition parametric settings, magnetron sputtering makes a great asset in building up solar cells layers, thermoelectric generators and nanostructured sensors [20–22].

Post–deposition annealing enables the stacked layers to react between each other. Moreover by adding extra S and/or Sn the targeted stoichiometry can be achieved. For CTS we are looking for a specific stoichiometry of 33.34% Cu, 16.16% Sn and 50% S [5, 23]. A high PCE aced in CTS requires careful considerations of secondary phase formation mitigations. Cu_xS and Sn_xS_y are some of the main secondary phases that co-exist with the main Cu_2SnS_3 phase [24]. Reducing or eliminating the occurrence of these unwanted phases can help achieving high performing CTS-based solar cells.

This paper provides a thorough analysis of the influence of secondary phases on the structural, morphological, compositional and optical properties of CTS thin films. Optimization methods for secondary phase reduction growth alongside with those of the analysis of secondary phase-dependent results are long–sought targets of our work beforehand.

2. MATERIALS AND METHODS

Three sets of samples deposited on soda lime glass (SLG) substrates are the main subject of the present study. Using the following stacking order: 400 nm of SnS_2 as a first layer, afterwards a 200 nm layer of Cu was coated on top of the SnS_2

film. The employed device is a Gencoa 3G Circular Magnetron array coupled to T&C Power Conversion AG 0313 RF (Radio Frequency) sources. During each deposition, the Argon (Ar) flow is maintained at 30 SSCM (standard cubic centimeters per minute) and the deposition power applied on the circular magnetron guns was set to 21 W and 30 W for the SnS_2 and the Cu layers, respectively. These power values have to be maintained to their pre-ignitions values in order to keep the plasma discharge intact. The SnS_2 first layer's deposition rate was set to 0.5 Å/s, while the Cu layer deposition rate was 0.245 Å/s. The distance between the target and the samples was set to 12 cm for each magnetron target. To achieve a given uniformity, homogeneity and isotropy of the elemental spread on the substrate, we opted for a steady substrate holder rotation. The value of the pressure inside the chamber was 6×10^{-3} Torr during deposition. The deposition is made step by step without opening the magnetrons' chamber door.

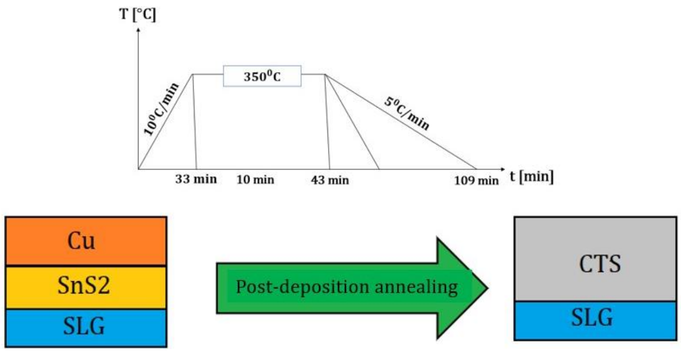

Fig. 1 – Post-deposition annealing process scheme and stacked layers diagram.

Post-deposition annealing treatments enable boundary reactions between the two thin layers, thus enhancing the stability of their chemical composition. This process is carried out in low vacuum conditions with a steady argon flow using a GSL 1600X tubular furnace. By adding extra S and/or Sn, a closer elemental concentration to the stoichiometric standard can be obtained. This process is carried out in low vacuum conditions around 10^{-2} Torr. The temperature inside the furnace rises from room temperature with a constant growth rate of 10°C/min until it reaches a steady plateau of 350°C for 10 minutes. The cooling slope is shallower, the temperature decreasing rate being half of the growth rate, namely 5°C/min. The entire process spans over 109 minutes to be completed. Each sample was annealed in a distinctive atmosphere in terms of elemental powder concentration ratios: one sample in 1 g of S, the second in 1.5 g of Sn and the third in both S (1 g) and Sn (0.5 g). Figure 1 presents the schematic diagrams depicting the stacked material layers and the post-deposition annealing temperature (T) *vs* time (t) graph.

Scanning electron microscope (SEM) from Zeiss EVO 50 XVP was employed to inspect the morphological surface structure of the films. The scanning electron microscope was paired with and EDS (energy-dispersive spectroscopy) device from Brucker in order to study the elemental composition of each sample.

In order to comprehensively understand the CTS crystalline structure and dimensional calculation, Grazing Incidence X-ray Diffraction (GIXRD) measurements were conducted with a Rigaku SmartLab X-ray diffractometer. The emitted CuKα radiation wavelength was about 1.5406 Å, under a 0.5° incidence angle. With a pre-set Bragg Brentano technique, the bouncing detector was calibrated to move with an angular velocity of 1.8 grad/min or $\omega = 5.236 \times 10^{-5}$ rad/s.

For a precise phase purity identification and secondary phases determination, a Jobin-Yvon Raman coupled confocal Olympus 100 × microscope spectrometer was employed to record Raman spectras. The CTS films were irradiated with the spectrometer's incorporated He-Ne laser calibrated to a 633 nm wavelength and a 5% emission input power.

A V-VASE Woollam Spectroscopic Ellipsometer equipped with a high-pressure Xenon discharge lamp incorporated in an HS-190 monochromator was used to provide the required transmission spectra. The conventional wavelength range of the apparatus falls between 350 nm and 1700 nm. The optical bandgaps were then calculated using the Tauc Plot method [26].

3. RESULTS AND DISCUSSIONS

Figure 2 exhibits the surface morphology of each sample depending on the chosen annealing atmosphere. These SEM images show different grain sizes and structures in all three CTS films, which can be explained by the presence of secondary phases. However, no cracks or voids were observed, which means that the surface morphologies are seemingly dense and compact.

The EDS measurements delivered the elemental composition data. Figure 3a displays the peak spread over the entire energy energy range. In all three samples, Cu, S and Sn are detected. We also notice arising Si and Ca peaks, as inherent constituents of the SLG substrate. Next, after calculating the concentration ratios of each element, we designed the Cu-Sn-S ternary diagram displayed in Fig. 3b. The light green dot represents the ideal stoichiometric values. It is worth mentioning that while all three samples are close to the intended stoichiometry, the closest sample to the ideal stoichiometric value was the film thermally treated in 1.5 g of S. These deviations from the targeted compositions come from the obvious Cu excess and lower Sn and S concentration. Sn and S are known to be very volatile elements, therefore their reduced concentration arises from the evaporation encountered during the annealing [5, 27]. As an observation, we note that our structures are prone to the formation of CuS and SnS secondary phases [5].

The GIXRD diffractograms are shown in Fig. 4a. The peaks at 28.40°, 47.20° and 56.06° in the three difractograms belong to the monoclinc CTS phase following the ICDD card (04-010-5719). In order to identify the coexisting secondary phases, the ICDD (00-006-0464) and (00-039-0354) cards of CuS and SnS secondary phases, respectively, were superimposed over the graphs, as it can also be observed in Fig. 4a [28]. Besides the CTS phase, peaks corresponding to the CuS phase were also detected in all films identified by the peaks at 2θ = 29.27°, 31.78° and 47.94°, while the signature of the SnS phase was found by the peaks at 2θ = 45.49° and 59.34°, with an additional peak at 27.47° in the film annealed in 1 g S and 0.5 g Sn.

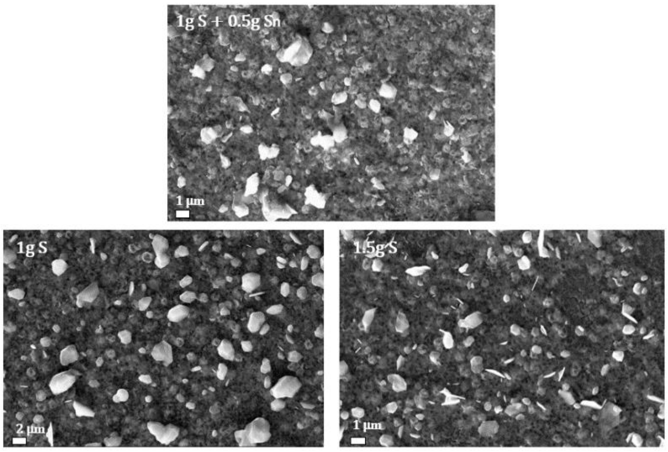

Fig. 2 – SEM images of the CTS (SLG/SnS_2/Cu) samples annealed in different atmospheres. Each image comprising one of the three films has denominated on the upmost left corner the elemental powder concentration corresponding to the appropriate annealing treatment.

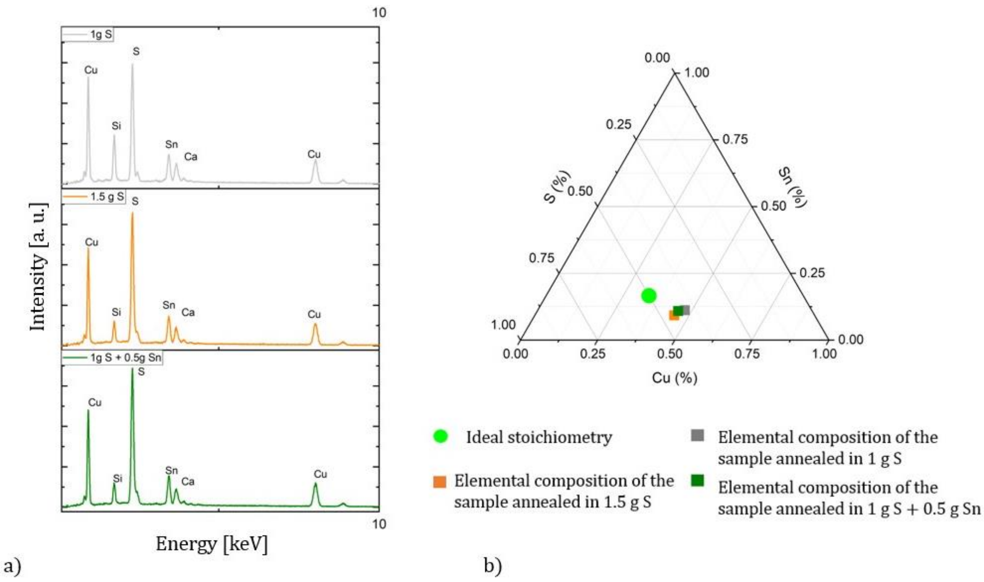

Fig. 3 – Elemental composition: a) EDS elemental spectra; b) ternary phase diagram.

The crystallite average size *D*, was computed using the Scherrer equation [29]:

$$D = \frac{K\lambda}{\beta\cos\theta} \tag{1}$$

where *K* is the shape factor, taken by default as 0.9 [30], $\lambda = 1.5406$ Å is the wavelength of the incident CuKα radiation and β stands for the line broadening at half the maximum intensity (FWHM) as given by the Lorentzian peak fit and θ is the diffraction maxima Bragg angle. However, due to the contribution of instrumental broadening to the estimated values of *D*, we employed a modified Scherrer equation that also accounts for these broadenings next to the ones associated to the peak Lorentzian fit and the CuKα wavalength correction [31]. Figure 4b reveals the average crystallite size for each analysed sample, namely 10.08 nm, 10.30 nm and 10.95 nm.

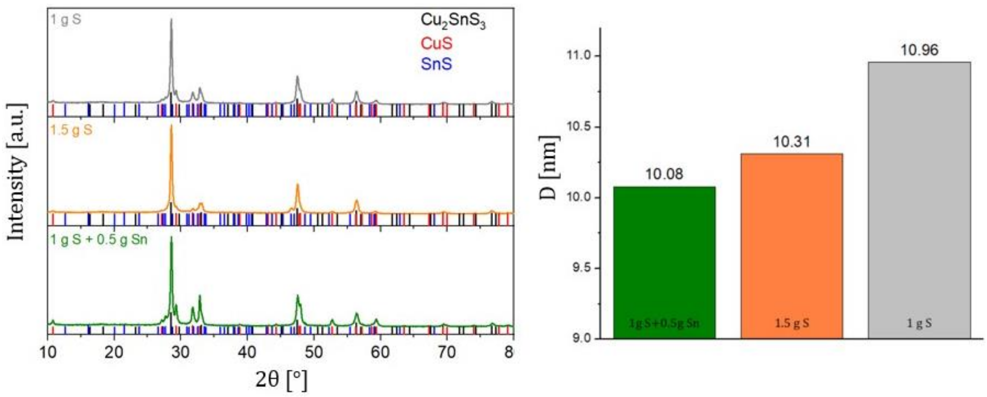

Fig. 4 – X-ray diffraction analysis: a) GIXRD results over ICDD spectra and b) average crystallite size.

Raman spectroscopy was employed as a complementary tool to detect the presence of secondary phases. Figure 5 displays the recorded Raman Spectra of the CTS samples annealed in different heat treatment atmospheres. The main peaks for all CTS films align at the same wavelength, proving once more, alongside the GIXRD plots, that CTS is the dominant phase in all films. The Raman peaks at 290, 330 and 350 cm^{-1} belong to the CTS phase. These values are similar to the literature [32]. As a strong indicator that the annealed samples have the same structure with a few differences in elemental concentrations, the Raman shifts figure points out the same secondary phases labeled in the previous discussions. Hence, one can observe the peak at 474 cm^{-1} corresponding to the CuS phase, alongside with the one of SnS at 320 cm^{-1}. The SnS peak is more visible in the Raman spectra of the sample annealed in S and Sn atmosphere.

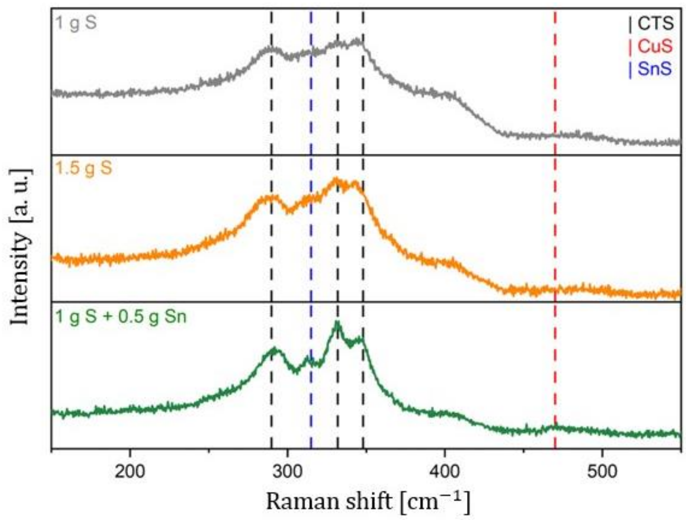

Fig. 5 – Raman spectra of the annealed samples.

The optical bandgaps of the CTS films are calculated using the Tauc Plot method [26, 33]. After subtracting the absorbance (*A*) of each film from the raw transmission (*T*) spectra, the absorbance coefficient can be computed deriving it from the Beer-Lambert law [34]:

$$\alpha = \log\left(\frac{1}{T}\right) = \log\left(1 + \frac{A}{T}\right) \quad (2)$$

Further, we use the Tauc Plot assigned formula:

$$(\alpha h\nu)^{1/n} = C\left(h\nu - E_g\right) \quad (3)$$

where $h\nu$ is the incident photon energy, the exponent $1/n$ describes the transition type inside the analysed semiconducting sample, C is a numerical constant and E_g is the bandgap. CTS thin films exhibit direct allowed transitions, therefore n is 1/2.

Figure 6 displays the three graphical representations of $(\alpha h\nu)^{1/n}$ *versus* $h\nu$. The bandgaps assigned to the CTS samples are 1.01 eV, 1.17 eV and 1.04 eV, corresponding to the films annealed in 1 g S, 1.5 g S, and respectively 1 g S + 0.5 g Sn. These values are in accordance with the afore-mentioned theoretical range falling between 0.8 and 1.7 eV [6]. While all three values are close to 1 eV, the arising minor differences occur due to different elemental compositions. Despite the presence of several secondary phases, their contribution to the found bandgaps is small, CTS structures being deemed as suitable absorber layers for photovoltaic studies and applications.

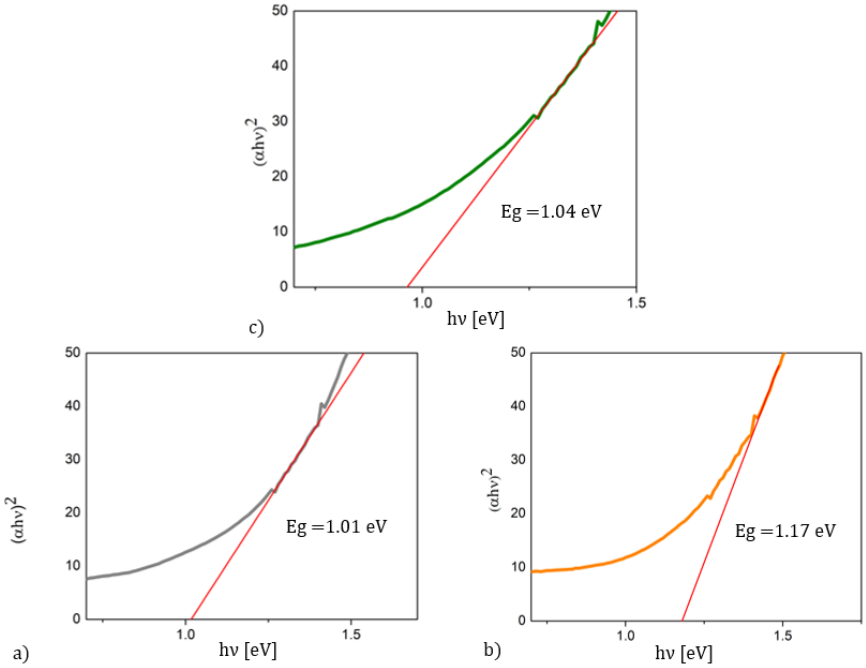

Fig. 6 – Tauc plots used to infer optical bandgaps of the CTS films anneled in:
a) 1 g S; b) 1.5 g S; c) 1 g S + 0.5 g Sn.

4. CONCLUSIONS

In summary, we have synthesized CTS films by annealing SLG\SnS_2\Cu stacks in different atmospheres of 1 g S, 1.5 g S and 1 g S + 0.5 g Sn. This study was conducted with the objective to investigate the formation and impact of secondary phases on the properties of CTS absorber layers. SEM images revealed non-uniform surfaces in all samples due to the coexistence of secondary phases, while EDS measurements exhibited off-stoichiometric compositions in the three films. GIXRD and Raman spectroscopy showed that the main phase in the three films is Cu_2SnS_3 phase, which is accompanied by CuS and SnS secondary phases. The optical bandgaps of the samples were estimated to vary between 1.01 and 1.17 eV. The presence of these secondary phases can be harmful to the performances of the CTS-based solar cells, therefore, it is mandatory to optimize the deposition and annealing parameters in order to prevent their formation.

Acknowledgements. The authors acknowledge the financial support provided by the Romanian Government through the Executive Unit for Financing Higher Education, Research, Development, and Innovation (UEFISCDI), under the Romanian Ministry of Research, Innovation, and Digitalization. This support was received within the framework of the following projects: PN-III-P1-1.1-PD-2021-0240 (contract no. PD 41/2022) and Core Program PC3-PN23080303.

REFERENCES

1. M. Suhail, H. Abbas, Mohd.B. Khan, and Z.H. Khan, J. Nanopart. Res. **24**(7), 142 (2022).
2. M.Y. Zaki, F. Sava, I.D. Simandan, A.T. Buruiana, C. Mihai, A. Velea, and A.C. Galca, Materials Science in Semiconductor Processing **153**, 107195 (2023).
3. L.L. Baranowski, P. Zawadzki, S. Lany, E.S. Toberer, and A. Zakutayev, Semicond. Sci. Technol. **31**(12), 123004 (2016).
4. Y. Shen, C. Li, R. Huang, R. Tian, Y. Ye, L. Pan, K. Koumoto, R. Zhang, C. Wan, and Y. Wang, Sci. Rep. **6**(1), 32501 (2016).
5. M.Y. Zaki, F. Sava, I.D. Simandan, A.T. Buruiana, C. Mihai, A. Velea, and A.C. Galca, Sci. Rep. **12**(1), 7958 (2022).
6. M.A. Olgar, Superlattices and Microstructures **138**, 106366 (2020).
7. S. Rahaman, M.K. Singha, M.A. Sunil, and K. Ghosh, Superlattices and Microstructures **145**, 106589 (2020).
8. J.J. Chaudhari, S. Patel, and U.S. Joshi, IOP Conf. Ser.: Mater. Sci. Eng. **149**, 012165 (2016).
9. D. Tiwari, T.K. Chaudhuri, T. Shripathi, and U. Deshpande, Journal of Physics and Chemistry of Solids **75**(3), 410–415 (2014).
10. E.S. Hossain, P. Chelvanathan, S.A. Shahahmadi, K. Sopian, B. Bais, and N. Amin, Current Applied Physics **18**(1), 79–89 (2018).
11. W. Liu, H. Li, B. Qiao, S. Zhao, Z. Xu, and D. Song, Solar Energy **233**, 337–344 (2022).
12. J. Fu, P.W.K. Fong, H. Liu, C.-S. Huang, X. Lu, S. Lu, M. Abdelsamie, T. Kodalle, C.M. Sutter-Fella, Y. Yang, and G. Li, Nat. Commun. **14**(1), 1760 (2023).
13. S.A. Vanalakar, G.L. Agawane, A.S. Kamble, C.W. Hong, P.S. Patil, and J.H. Kim, Solar Energy Materials and Solar Cells **138**, 1–8 (2015).
14. P.G. Suryawanshi, B.M. Babar, A.A. Mohite, U.T. Pawar, A.G. Bhosale, and H.D. Shelke, Materials Today: Proceedings **43**, 2682–2688 (2021).
15. A. Kanai, H. Araki, A. Takeuchi, and H. Katagiri, Phys. Status Solidi B **252**(6), 1239–1243 (2015).
16. G. Sunny, T. Thomas, D.R. Deepu, C.S. Kartha, and K.P. Vijayakumar, Optik **144**, 263–270 (2017).
17. M.R. Pallavolu, C.-D. Kim, V.R. Minnam Reddy, S. Gedi, and C. Park, Solar Energy **188**, 209–217 (2019).
18. F. Sanchette and A. Billard, Coatings **10**(11), 1072 (2020).
19. P.J. Kelly and R.D. Arnell, Vacuum **56**(3), 159–172 (2000).
20. S. Gulkowski and E. Krawczak, Coatings **10**(8), 791 (2020).
21. K. Takayama and M. Takashiri, Vacuum **144**, 164–171 (2017).
22. X. Pang, Q. Zhang, Y. Shao, M. Liu, D. Zhang, and Y. Zhao, Sensors **21**(4), 1130 (2021).
23. M.Y. Zaki, F. Sava, I.-D. Simandan, A.T. Buruiana, I. Stavarache, A.E. Bocirnea, C. Mihai, A. Velea, and A.-C. Galca, ACS Omega **7**(27), 23800–23814 (2022).
24. E. Ketenci Ozsoy, F. Atay, and O. Buyukgungor, Solar Energy **214**, 179–188 (2021).
25. Y. Dong, J. He, X. Li, Y. Chen, L. Sun, P. Yang, and J. Chu, Journal of Alloys and Compounds **665**, 69–75 (2016).
26. J. Tauc, Materials Research Bulletin **3**(1), 37–46 (1968).
27. I.Y. Kim, J.Y. Lee, U.V. Ghorpade, M.P. Suryawanshi, D.S. Lee, and J.H. Kim, Journal of Alloys and Compounds **688**, 12–17 (2016).
28. E.L. Barbedo, P.H. Gonçalves, M.S. Lamoglia, A.M.P. Pontes, B.H. Bastos Kuffner, G.F. Gomes, and G. Silva, Mat. Res. **24**(5), e20210054 (2021).
29. A. Monshi, M.R. Foroughi, and M.R. Monshi, WJNSE **02**(03), 154–160 (2012).
30. A.L. Patterson, Phys. Rev. **56**(10), 978–982 (1939).
31. M.Y. Zaki, K. Nouneh, M.E. Touhami, E. Matei, P. Badica, M. Burdusel, C.C. Negrila, M. Baibarac, L. Pintilie, and A.C. Galca, Phys. Scr. **95**(5), 054001 (2020).
32. P.A. Fernandes, P.M.P. Salomé, and A.F. Da Cunha, Phys. Status Solidi (c) **7**(3–4), 901–904 (2010).
33. P. Makuła, M. Pacia, and W. Macyk, J. Phys. Chem. Lett. **9**(23), 6814–6817 (2018).
34. J.D.J. Ingle, S.R. Crouch, New Jersey, Prentice Hall, 1988.